Volume 1 | Number 1 | Jan 2013 | Pages 1–100

PCCP

Physical Chemistry Chemical Physics
www.rsc.org/pccp

ROYAL SOCIETY OF CHEMISTRY

ROYAL SOCIETY OF CHEMISTRY

www.rsc.org/pccp

ARTICLE TYPE

Designing and Understanding Permanent Microporosity in Liquids [†]

Gavin Melaugh,[a] **Nicola Giri,**[b] **Christine E. Davidson,**[b] **Stuart L. James,**[b] **and Mario G. Del Pópolo,**[*c]

Standard microporous materials are typically crystalline solids that exhibit a regular array of cavities of uniform size and shape. Packing and directional bonding between molecular building blocks give rise to interstitial pores that confer size and shape-specific sorption properties to the material. In the liquid state interstitial cavities are transient. However, permanent and intrinsic "pores" can potentially be built into the structure of the molecules that constitute the liquid. With the aid of computer simulations we have designed, synthesised and characterised a series of liquids composed of hollow cage-like molecules, which are functionalised with hydrocarbon chains to make them liquid at accessible temperatures. Experiments and simulations demonstrate that chain length and size of terminal chain substituents can be used to tune, within certain margins, the permanence of intramolecular cavities in such neat liquids. Simulations identify a candidate "porous liquid" in which 30% of the cages remain empty in the liquid state. Absorbed methane molecules selectively occupy these empty cavities.

1 Introduction

The prospect of engineering permanent porosity into the liquid state is of fundamental interest and potentially, in the longer term, may lead to novel separation and storage technologies, and customised reaction media.

Permanent microporosity is currently associated with solid state materials of various kinds, including zeolites, metal-organic frameworks, organic polymers and, more rarely, crystals of discrete organic molecules.[1–4] By contrast, in liquids far from their critical points, porosity is predominantly limited to small vacancies which are generated transiently between the molecules as they tumble.[5,6] Although these cavities are mainly small, short-lived, and irregularly-shaped, they strongly influence the solubilising characteristics of the liquid.[7] In particular, in addition to the specific solute-solvent interactions, the solvation of a solute depends on the energy required to generate a cavity of appropriate size. The ability to tune the porosity present in the liquid state is therefore desirable in order to achieve greater control over solubility, diffusion, and perhaps reactivity. For example, increased solubility, and even size and shape-selective solubility, might be achieved by this approach.

A generic molecular design for a liquid bearing permanent cavities consists of a rigid empty core structure,[4] which defines an *intrinsic cavity*, and which is rendered liquid at accessible temperatures by the addition of long flexible chains to the outside.[8] Clearly, of key interest would be the propensity of the chains to occupy the cavities. This aspect can be expected to depend on the chain length, flexibility, and the bulk of the chain terminal group.

In this work a series of materials of this general design has been modelled with the aid of computer simulations, synthesised and investigated through physical characterisation. Each material consists of a rigid iminospherand cage core to which twelve hydrocarbon chains have been added. We have considered chains which range from five up to twenty-two carbon atoms including linear chains but also chains with a degree of terminal branching (see Fig. 1 for the specific materials prepared and modelled). From this study, materials with melting points ranging from 313 K (40°C) to 429 K (156°C) have thus been prepared. Computer simulations give detailed insight into the liquid structures of these materials, and reveal the influence of chain length and branching on fluidity as well as intrinsic porosity. A candidate porous liquid is identified in which 30 % of the cage cavities remain accessible in the liquid state. Simulations also show that methane dissolved in this liquid selectively occupies the empty intrinsic cavities.

The cage molecules described here are related to similar host types including cryptophanes,[9–12] which have in some cases been studied when dissolved in bulky solvents such that the central cavity is almost certainly unsolvated.[9,10] However, the persistence of actual cavities has not been proven in such

---

*[a] Atomistic Simulation Centre, School of Mathematics and Physics, Queen's University Belfast, BT7 1NN, UK*
[b] School of Chemistry and Chemical Engineering, Queen's University Belfast, BT9 5AG, UK
[c] CONICET e Instituto de Ciencias Básicas, Universidad Nacional de Cuyo, Mendoza, Argentina; & Atomistic Simulation Centre, School of Mathematics and Physics, Queen's University Belfast, BT7 1NN, UK. E-mail: m.del-popolo@qub.ac.uk

systems to our knowledge.

2 The experimental picture
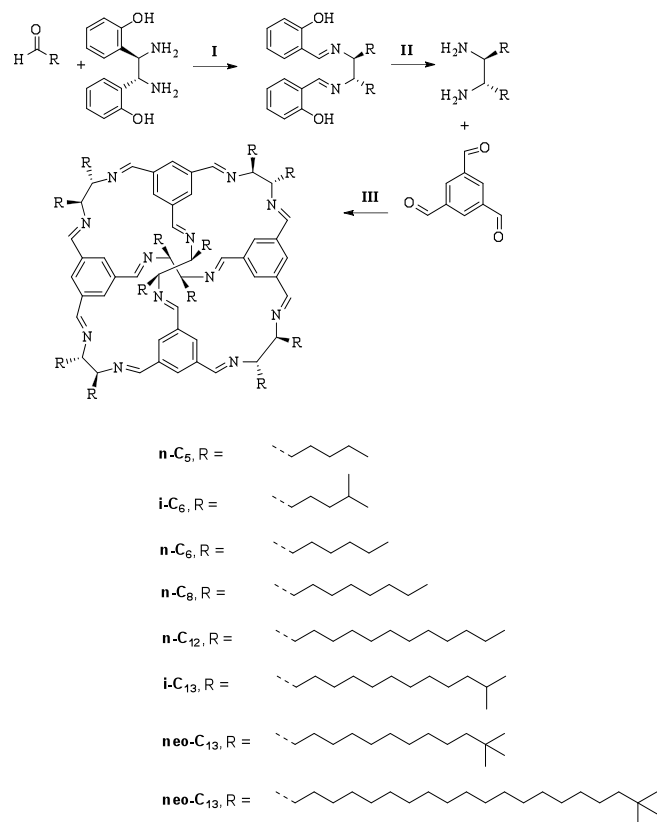
Fig. 1 General synthetic pathway for organic cages n-C$_{12}$, iso-C$_{13}$ and neo-C$_{14}$, and the naming scheme for all alkylated cage materials discussed in this work.

The syntheses of alkylated cages n-C$_5$, n-C$_8$, iso-C$_6$ and n-C$_6$ have been described in a previous publication.[13] Three longer-chain examples, n-C$_{12}$, iso-C$_{13}$ and neo-C$_{14}$, were prepared as part of the current study in the expectation that they should have lower melting points than the previously prepared cages and, more specifically, to complement relevant aspects of the modelling studies presented below. The synthetic strategy involved the condensation between 1,3,5-triformylbenzene and the appropriate diamine bearing the alkyl chains.[13] Detailed experimental procedures and characterising data for all products and intermediates are given in the Supplementary Information. Some general observations on the cage formation step are also included here. A standard synthetic method described in the literature for cages bearing small substituents involves addition of a diamine to the 1,3,5-triformylbenzene which is dissolved in dichloromethane. The

reaction is allowed to stir at room temperature for 12hrs and the product can be purified by crystallisation.[14] However, in the current work, this method was unsuccessful for the di-amines bearing longer and/or bulkier alkyl groups. Reaction between bulky diamines such as (R,R)-1,2-diamino-1,2-diphenylethane and 1,3,5-triformylbenzene under these conditions has also been reported to be unsuccessful, giving only a mixture of products.[14] In the current work, slow addition of the diamine as well as high dilution conditions were also investigated but again without success. However, heating the reactions to reflux in chloroform containing a catalytic amount of trifluoroacetic acid did successfully afford the target cages. It has also been reported elsewhere that a catalytic amount of acid can cause interlocking of this type of cage to occur.[15] Fortunately, this interlocking was not observed in the current work presumably because it is sterically prevented by the long alkyl substituents. It was also found that the use of a small excess of diamine resulted in higher yields of the cages. Completion of the cage-formation reaction was assessed by monitoring the reactions by ^{1}H-NMR spectroscopy. In particular, the distinctive protons for the imine and the aromatic groups in the highly symmetrical final product are observed at 8.0 ppm and 7.8 ppm respectively. During cage formation these peaks grow in intensity whilst other peaks in this region, which are presumably due to intermediate oligomers or partially formed cages, slowly decrease. In the current work several days were required for complete formation of the cages. The products could not be obtained in sufficiently pure form directly by crystallisation, and required column chromatography with hexane-ethyl acetate or benzene-ethyl acetate as eluent for purification. Some decomposition was suspected to have occurred on the column for these longer-alkyl chain cages and isolated yields for the cages were 27 % (n-C$_{12}$), 35 % (iso-C$_{13}$), and 59 % (neo-C$_{14}$). The products were characterised by a combination of ^{1}H NMR, ^{13}C NMR, MALDI-MS, microanalysis and thermogravimetric analysis. All data were in accord with the expected structures (see Supplementary Information).

All three new materials, n-C$_{12}$, iso-C$_{13}$ and neo-C$_{14}$ were found to be soft, waxy solids at room temperature. Their melting behaviours were assessed both visually by hot stage microscopy, and thermally by differential scanning calorimetry (DSC). Visually, on heating all changed from waxy solids to free-flowing liquids with melting temperatures estimated as 313.15 K (40°C) for n-C$_{12}$ and iso-C$_{13}$, and 328.15 K (55°C) for neo-C$_{14}$. On subsequent re-cooling, all three materials retained the high transparency of their liquid phases rather than returning to their initial waxy appearance. It is notable that, in contrast to the shorter chain analogues n-C$_5$ (M.P. 429 K / 156 °C) and iso-C$_6$ (M.P. 471 K / 198 °C) in which terminal branching of the chains markedly increases the melting point,[13] chain branching in these materials has much less ef-

fect. This is intuitively reasonable since the structural effect of the branching is proportionately less in these longer chains. n-C_{12} and iso-C_{13} behaved similarly to each other under DSC analysis. On heating, n-C_{12} showed a broad endothermic melting transition between ca. 308.15 - 318.15 K (35-45 °C).[16] However, on cooling and on subsequent heating-cooling cycles the same sample showed no evidence of a glass transition or re-melting. This is consistent with the visual observation that the material appears not to return to its initial state upon cooling, at least within the time frame of these experiments. The observation of melting and glass transitions can of course be sensitive to heating or cooling rates. iso-C_{13} showed very similar behaviour with a broad melting transition from ca. 308.15 - 318.15 K (35-45 °C), and no evidence of glass transitions or melting on subsequent cooling or further heating-cooling cycles. Upon heating, neo-C_{14} exhibited a small endothermic transition at 326.15 - 328.15 K (53-55°C) corresponding to the melting transition observed visually. This feature is somewhat sharper and occurs at higher temperature than the corresponding melting transitions in n-C_{12} and iso-C_{13}. Computer simulation results discussed below provide, among other things, some interpretations for this difference in melting behaviour.

3 Computational methods

Molecular Dynamics (MD) simulations were performed with GROMACS-4.5.3,[17] using an empirical force-field developed on the basis of the OPLS-AA and OPLS-UA models.[18,19] Molecules were modelled as a collection of Lennard-Jones particles connected by stretching, bending, and torsional potentials. All atoms forming the cage core were explicitly accounted for, and some of them carried a partial point charge.[20] Methyl and methylene groups on the hydrocarbon chains were coarse-grained into neutral united-atom beads (see Fig. 2), a description that is fully justified by the remarkable performance of united-atom models in predicting the phase-diagram and mixing properties of aliphatic hydrocarbons.[21] In fact, as discussed in the following sections, cohesion in the present systems stems from dispersion forces with Coulombic interactions playing a minor and secondary role.[22]

In connection with the present model, we notice that Holden et al. have recently developed an all-atom force-field that reproduces the molecular packing, crystal structure, and gas sorption properties of high-melting iminospherand cages bearing smaller and less flexible substituents.[23,24] Combining the model of reference[23] with the one proposed here for low melting alkylated cages, may in principle lead to an all-inclusive force-field suitable for simulating a wider range of substituted iminospherand cages.

Starting configurations consisting of 64 molecules enclosed in a cubic simulation box were generated and equilibrated at
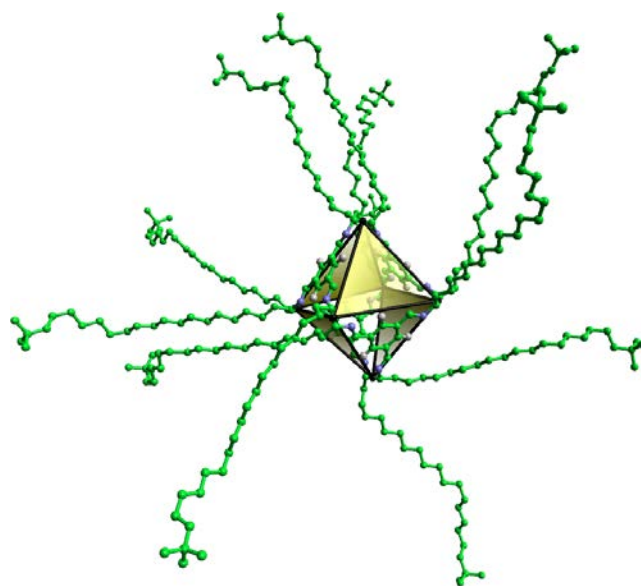

Fig. 2 United atom representation of a neo-C_{22} molecule. The octahedron highlights the hollow cage core. The access windows are featured as transparent yellow planes.

high temperature. Each system was then annealed from 600 K to 200 K at a constant rate of 4 K/ns and a pressure of 1 atm. Configurations sampled along the annealing trajectory were used as starting points for 100 ns-long isobaric-isothermal (NPT) MD simulations. The NPT ensemble conditions were imposed by combining a Nose-Hoover thermostat[25,26] with a Parrinello-Rahman barostat,[27] with time constants of 0.1ps and 1ps, and an integration time step of 2 fs. Lennard-Jones interactions were cut off at 1.4 nm, while Coulomb forces were computed using the smooth particle mesh Ewald technique.[28] A relative strength of 10^{-5} (`ewald_rtol`) was used for the Ewald-shifted direct potential at 1.7 nm, together with a set of k-vectors with a maximum length of 15 in reciprocal space. Structural, dynamical and thermodynamic properties were calculated from a sample of 2000 configurations drawn from the NPT trajectories.

The free energy profiles reported in 5 were computed by Umbrella Sampling (US),[29] using a restraining potential of the form $\frac{K_n}{2}(r - r_n^{eq})$, where r represents a reaction coordinate, K_n is the force constant, and r_n^{eq} is the reference position of the umbrella potential in the n-th window. In each window the system was equilibrated at constant P and T during 10 ns. Production runs were extended for another 15ns. The final free energy profiles were recovered using the Weighted Histogram Analysis Method (WHAM).[30,31]

Additional technical details on MD and US simulations are provided as Supplementary Information.
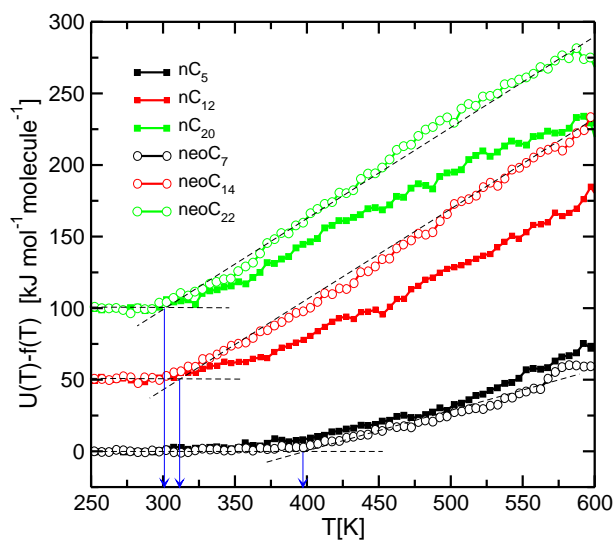
Fig. 3 Potential energy per molecule versus temperature. Annealing rate 4 K ns^{-1}. A linear function, $f(T) = a + bT$, has been subtracted from each $U(T)$ curve. The parameters a and b are reported in the Supplementary Information.

4 Energetics, fluid structure and dynamics

The evolution of thermodynamic properties during the annealing scans provide a first point of comparison with experimental observations. Fig. 3 shows the configurational contribution to the internal energy as a function of temperature for n-C$_5$, n-C$_{12}$, n-C$_{20}$, neo-C$_7$, neo-C$_{14}$, and neo-C$_{22}$. The relevant information contained in these curves has been highlighted by subtracting from the raw data a linear function, $f(T) = a + bT$, fitted to the points lying on the 250-300 K interval.[32] Although the thermal decomposition point of these materials is around 500 K,[13] the simulated annealing runs were started at 600 K in order to guarantee good initial mixing.

In all the systems investigated, the internal energy, $U(T)$, shows a low- and a high-temperature linear regime separated by a smooth and relatively broad crossover region that encloses the measured melting points. Such regions can be identified from the intersection of the dashed lines in Fig. 3. Increasing the length of the alkyl chains clearly decreases the transition temperature, from ∼400 K in n-C$_5$/neo-C$_7$, to 310-320 K in n-C$_{12}$/neo-C$_{14}$, and 300-310 K in n-C$_{20}$/neo-C$_{22}$. The size of the terminal groups affects mostly the change of slope of $U(T)$ across the transition and increases slightly the crossover temperature. For example, in n-C$_{12}$ the transition occurs near 300 K, which compares well with its experimental melting point of 313 K; while in neo-C$_{14}$ the crossover falls near 320 K, not far away from the measured melting point of 328 K. The effect of the terminal group on the internal energy is pronounced in the long-chain systems (n-C$_{20}$ vs. neo-C$_{22}$,
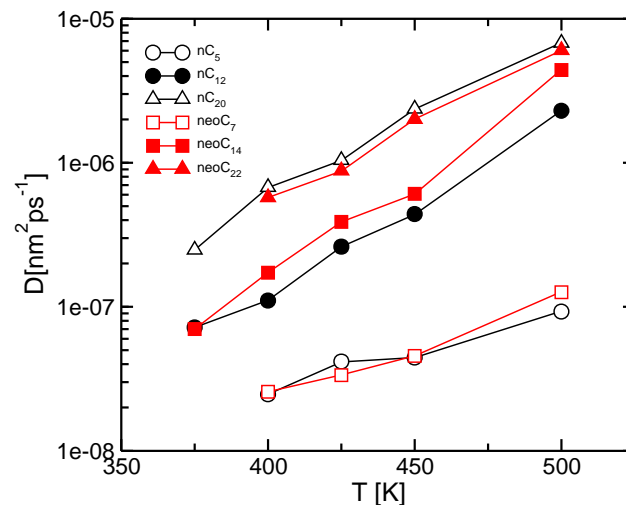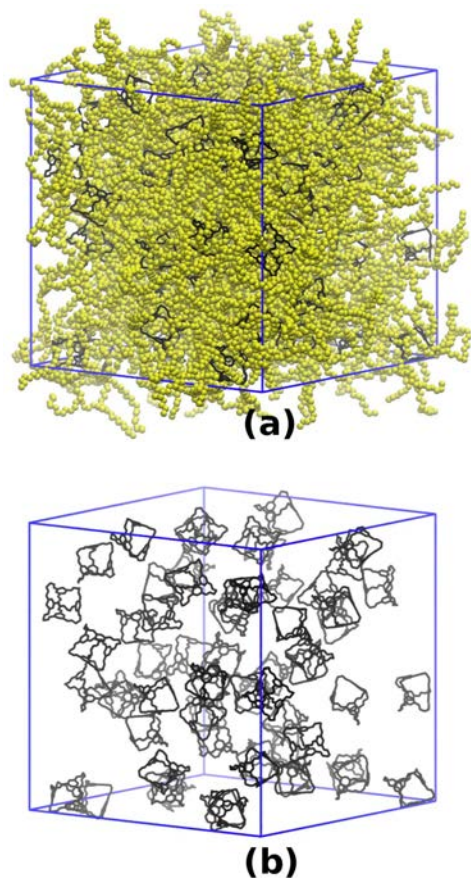

Fig. 4 Translational diffusion coefficients, D, as a function of temperature.

n-C$_{12}$ vs. neo-C$_{14}$), but is almost negligible in n-C$_5$ and neo-C$_7$.[33]

In every system investigated, the analysis of simulation snapshots at both sides of the crossover regions reveals a transition between a fluid phase and a disordered solid-like structure at low temperature. Such a scenario conforms with a glassification or defective solidification, as observed in simulations of liquids made of molecules with flexible substituents.[34] The weakness of the transitions in Fig. 3 could be exacerbated by the short time scale of our simulations, as compared with experimental solidification or glassification times, or could be seen as a manifestation of the complexity of these systems and of their phase behaviour.

The phase change is marked by a severe damping in the molecular motion. Translational diffusion coefficients, D, were calculated in order to quantify this effect and as a way to assess the fluid viscosity. Fig. 4 shows the values of D within the range of temperatures where systems are unambiguously fluid, and mean square displacements reach the expected diffusive regime within the time scale of the simulations (100 ns). In general, diffusion coefficients are low and in some cases comparable to those of molecular tracers in polymer melts (10^{-6} - 10^{-7} nm^2/ps),[35] or molecules in lipid bilayes (10^{-5} - 10^{-6} nm^2/ps).[36,37] It is also clear from the simulations that, within the range of temperatures explored, these liquids are fairly viscous, in agreement with rheological experiments performed on n-C$_8$.[13]
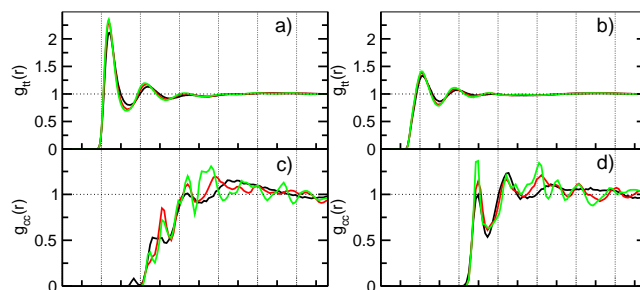
An important conclusion from Fig. 4 is that long hydrocarbon chains are effective in conferring fluidity to the iminospherand cages, in spite of increasing their molecular size and weight. For example, at 450 K D goes from 4.4 10^{-8} nm^2/ps for n-C$_5$ to 2.4 10^{-6} nm^2/ps for n-C$_{20}$, and a simi-

Fig. 6 Chain-chain radial distribution functions, $g_{tt}(r)$, for neo-C_{14} (panel a) and n-C_{12} (panel b) computed at 350, 400 and 500 K. Panels c) and d), cage-cage RDFs, $g_{cc}(r)$, for neo-C_{14} and n-C_{12} respectively, at 350, 400 and 500 K.

Fig. 5 Instantaneous configuration of the n-C_{20} system at T = 375 K. Whole molecules are shown in panel (a). Cage cores are exposed in panel (b) by removing the hydrocarbon chains.

lar trend could be drawn for the neo-C_7 / neo-C_{22} systems. The likely origin of this effect is the softening of the effective interaction potential between the cages,[38] due to the increasing conformational entropy of the chains as they get longer. In other words, the energy barriers separating the conformational states of the chains seem to be surmountable in the liquid phase, providing ready access to many more microstates in the case of long chains. This interpretation is supported by the distributions of chain lengths, as measured from the tip of the chain to the anchoring point to the cage, illustrated in Figure 7 of the Supplementary Information. For long chains these functions show two maxima separated by a local minimum that become less pronounced as the number of methylene beads increases, pointing to a greater flexibility of the chain. Moreover, a dynamic analysis of the chain-length fluctuations confirms that, during equivalent time spans, long chains perform longer excursions than the shorter ones.

Fig. 5 displays a typical configuration of the n-C_{20} system. Whole molecules are shown in panel (a), while panel (b)

shows only the cage cores. It is visually evident from this figure that hydrocarbon chains provide the medium in which the cage cores are suspended. The relative arrangement of atoms and molecules in this fluid, can be assessed from the site-site radial distribution functions (RDFs) of Fig. 6. Panels (a) and (b) show the RDFs between the chain terminal group, $g_{tt}(r)$, for neo-C_{14} and n-C_{12} at three different temperatures. In this case distances are measured from the second-last carbon atom of the chain, henceforth called the pivot.

Clearly, chain ends cluster together in the intermolecular space leading to a first prominent peak in $g_{tt}(r)$. The position and height of this first peak are modulated by the size of the terminal group, but chain length seems to have little effect on the shape of $g_{tt}(r)$.[39] Overall, chain-chain correlations are fairly short ranged, and the "liquid-like" character of $g_{tt}(r)$ is remarkably insensitive to temperature. In contrast, cage-cage RDFs measured from the geometric centres of the cage cores develop sharper features as temperature decreases. These functions, labeled as $g_{cc}(r)$, are shown for neo-C_{14} and n-C_{12} in panels (c) and (d) of Fig. 6. Given the size of these molecules , cage-cage correlations are generally weak and depend on the length of the hydrocarbon chains.

5   Chains can occupy the cage cavities

Hydrocarbon chains are effective at decreasing melting points and conferring fluidity. However, simulations reveal that the chain terminal groups can also occupy the intramolecular cavities and decrease the actual porosity of the system. This effect is modulated by the chain length and the size of the terminal groups.

Fig. 7 shows the average fraction of cages occupied by chain ends, $\langle x_{oc} \rangle$, as a function temperature for n-C_5, n-C_{12} and n-C_{20}, i.e. the molecules with non-branched chains. For the sake of calculating $\langle x_{oc} \rangle$, a cage was considered to be occupied when the pivot atom of a chain was within 2.5 Å from
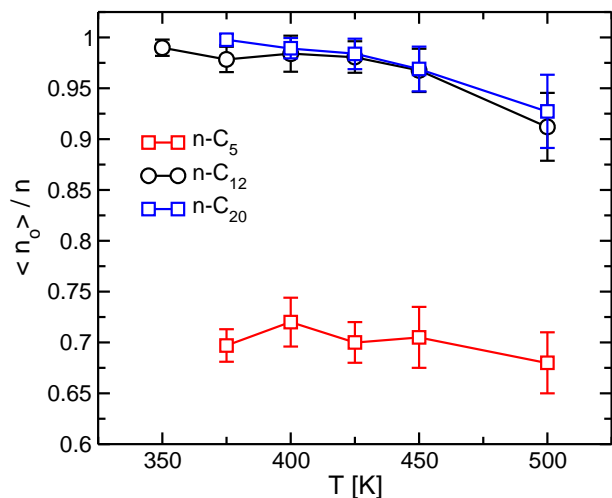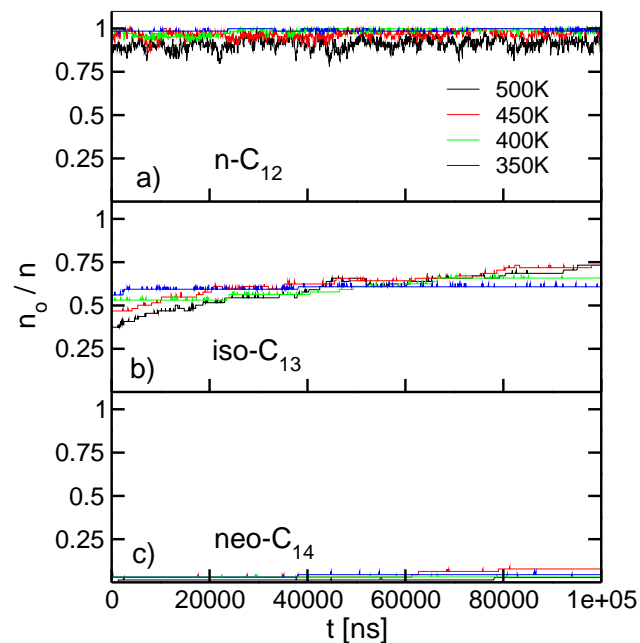
Fig. 7 Fraction of occupied cages, $\langle x_{oc} \rangle = \langle n_o \rangle / n$, in n-C$_5$, n-C$_{12}$ and n-C$_{20}$ as a function of temperature. The vertical, error-like, bars represent the equilibrium root mean square fluctuation of x_{oc}.

Fig. 8 Time evolution of the fraction of occupied cages, $x_{oc}(t) = n_o/n$, at various temperatures in n-C$_{12}$, iso-C$_{13}$ and neo-C$_{14}$

the cage centre. The long n-C$_{12}$ and n-C$_{20}$ chains readily penetrate through the cage windows, leading to 0 to 10 % of cages being empty in the 350-500 K temperature interval. On the other hand, the fraction of empty cages in the short-chained n-C$_5$ system, within the same temperature interval, is more than 30 %. Considering that the melting point of n-C$_5$ is $\sim$ 430 K (157°C), these results indicate that is possible to maintain open intra-molecular cavities in a neat liquid under accessible laboratory conditions. Therefore, n-C$_5$ can be considered as a permanently porous liquid.

The small change with temperature observed in $\langle x_{oc} \rangle$ suggests that enthalpy drives the tip of the chains inside the cages. Furthermore, the root mean square fluctuations of x_{oc}, represented by the vertical bars on top of the symbols of Fig. 7, show that the number of occupied cages fluctuates with time as chains visit different cages while molecules diffuse. This is also evident from Fig. 8, which compares the time evolution of x_{oc} in n-C$_{12}$, iso-C$_{13}$ and neo-C$_{14}$ at several temperatures.

In n-C$_{12}$, $x_{oc}(t)$ shows truly equilibrium fluctuations and no drift during a 100 ns simulation.[40] In fact, in all the straight chain systems (n-series) the activated $chain - out \rightleftharpoons chain - in$ events are so frequent that it is possible to compute the corresponding mean-first-passage times, τ. For example, at 350 K $\tau_{in \rightarrow out}$ is 15 ns in nC$_{20}$, 13 ns in nC$_{12}$, and 3 ns in n-C$_5$.[41] In general, longer chains lead to faster $chain - out \rightleftharpoons chain - in$ kinetics, something that can be attributed to the greater fluidity observed in these systems.

Fig. 8 also reveals that the size of the terminal group has a pronounced effect on the rate at which cages are occupied or emptied. In the medium sized iso-C$_{13}$ system, $x_{oc}(t)$ shows

a clear upward drift pointing to an overall free energy gain as the fraction of occupied cages increases (Fig. 8b). In the bulkier neo-C$_{14}$ system the fraction of occupied cages is low and remains practically constant during the course of the simulation (Fig. 8c). The remaining question is whether the neo-C$_{14}$ chains truly prefer to reside outside the cage, or whether the low fraction of occupied cages results from a long-lived metastable sate.

In order to investigate this point, the thermodynamic cost, $\Delta G(r)$, of bringing a chain-end up to a distance r from the centre of a cage was computed by umbrella sampling.[42] Fig. 9 shows the free-energy profiles for n-C$_5$, n-C$_{12}$, n-C$_{20}$, iso-C$_{13}$ and neo-C$_{14}$. In every case the free energy reaches a minimum, ΔG_{min}, when the chain is inside the cage ($r \sim 0$), while the $chain - out \rightleftharpoons chain - in$ kinetics is controlled by the activation barriers $\Delta G_{in \rightarrow out}^{act}$ and $\Delta G_{out \rightarrow in}^{act}$. By comparing the n-C$_5$, n-C$_{12}$ and n-C$_{20}$ curves, it is clear that the effect of chain length saturates at some point. In fact, the n-C$_{12}$ and n-C$_{20}$ curves are almost identical, while the well depth and activation barriers are lower in n-C$_5$. From the curves' parameters reported in 1, it can then be inferred that n-C$_5$ must show the highest fraction of empty cages, and that the turnover $chain - out \rightleftharpoons chain - in$ rate should be fast in all the straight-chain systems. All this is in agreement with the trends observed in Fig. 7 and Fig. 8a.

The iso-C$_{13}$ and neo-C$_{14}$ curves demonstrate that a moder-
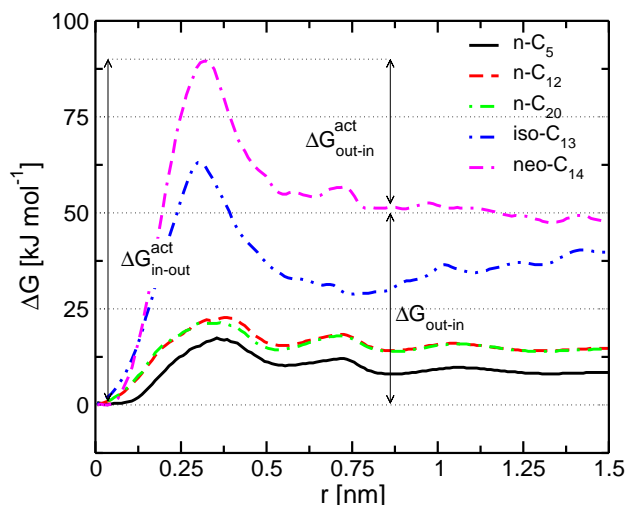
Fig. 9 Free energy cost, $\Delta G(r)$, of bringing a chain terminal group up to a distance r from the centre of the cage. Curves computed at 400 K for n-C$_5$, n-C$_{12}$, n-C$_{20}$, iso-C$_{13}$ and neo-C$_{14}$

Table 1 Free-energy well depth, $\Delta G_{out \to in}$; and barrier heights, $\Delta G^{act}_{in \to out}$ and $\Delta G^{act}_{out \to in}$, calculated from the profiles of Fig. 9. T = 400 K. Energy units: kJ mol^{-1}

	$\Delta G^{act}_{in \to out}$	$\Delta G^{act}_{out \to in}$	$\Delta G_{out \to in}$
n-C$_5$	17.5	9.3	-8.1
n-C$_{12}$	22.8	8.7	-14.1
n-C$_{20}$	21.5	7.6	-13.8
iso-C$_{13}$	63.1	34.2	-28.9
neo-C$_{14}$	89.5	41.8	-47.6

ate increase in the size of the terminal group, increases both the depth of the well and the height of the two activation barriers. The bulkiest neo-C$_{14}$ shows the strongest binding energy to the cage cavity, but the transitions between empty and occupied states should be the slowest among all the systems covered in 1. The immediate conclusion stemming from these results is that the low fraction of occupied cages observed in neo-C$_{14}$ (Fig. 8c) corresponds to a long-lived metastable state.

The results of the present section can be summarised in the following way: the fraction of intramolecular cavities that remain vacant in the liquid state, as well as the rate at which they are occupied/emptied, is controlled by the length of the alkyl-chains and the size of the terminal group. Perhaps, contrary to simple intuition, over long time scales, short tails and small terminal groups lead to a larger fraction of empty cages. The intramolecular cavity of our iminospherand cages is large enough to accommodate a bulky $-(CH_3)_3$ group, although cage occupation kinetics is slower in this case. It is also likely that terminal groups larger than $-(CH_3)_3$ will lead to a higher percentage of free cage cavities due to steric effects.

6 Cavity size distributions, relative porosity and selective gas sorption

Three representative materials were chosen for more detailed analysis. These were, specifically, neo-C$_{14}$ which has 100 % of cages empty over the timescale of the simulation, n-C$_5$ which has 30 % of cages permanently empty, and n-C$_{12}$ which has 0 % percent of cages empty.

Porosity in solids and liquids, associated with either perma-

nent or transient cavities, can be quantified by the fraction of the sample volume, $p(R)$, accessible to a rigid spherical probe of radius R.[5,6] That is to say,

$$p(R) = \frac{\langle V(R) \rangle}{V} \quad (1)$$

where V is the volume of the sample and $\langle V(R) \rangle$ is the part of it that, on average, can be accessed by the probe. Alternatively, $p(R)$ can be interpreted as an "insertion probability", because it measures the likelihood of inserting a hard sphere of radius R, at a random point in the liquid, without overlapping with any of the atoms in the sample. It must be noted that $p(R)$ does not provide information on the shape of the cavities, nor on the way cavities are arranged in the material.

In a liquid containing "hollow" structures, randomly inserted probes can either fall inside the molecular cavities, or in the pockets of free space between the molecules. The contribution from the molecular cavities to the overall volume sensed by the probe, can then be assessed from the "relative porosity",

$$W(R) = \frac{\langle V(R) \rangle}{\langle V_{exc}(R) \rangle} = \frac{p(R)}{p_{exc}(R)} \quad (2)$$

where $\langle V_{exc}(R) \rangle$ is the volume accessible to the probe excluding the intrinsic pore of the hollow molecules. For a given configuration of the system, $V_{exc}(R)$ is calculated in the same way as $V(R)$ but blocking all the cage cavities with a hard-sphere of radius 2.5 Å placed at their centre.

Fig. 10 shows $W(R)$ for neo-C$_{14}$, n-C$_{12}$ and n-C$_5$ at various temperatures. Each curve shows a maximum at a probe radius of 1.75 Å$-$2.25 Å. This indicates that the pore space, provided by the cage-cores, outcompetes the equally sized pores that occur through spontaneous density fluctuations in the intermolecular space. It should also be noticed that $W(R) \sim 1.0$ for probes larger than 2.5 Å or smaller than 1.0 Å, meaning that the cage cavities have little effect on the porosity of the fluid when sensed by very small or very large probes.

Another remarkable trend of the curves in Fig. 10 is that the size specificity effect of the molecular cage is more noticeable at low temperatures, as reflected by the increase in the peak height as the liquid is cooled. This is readily explained by the
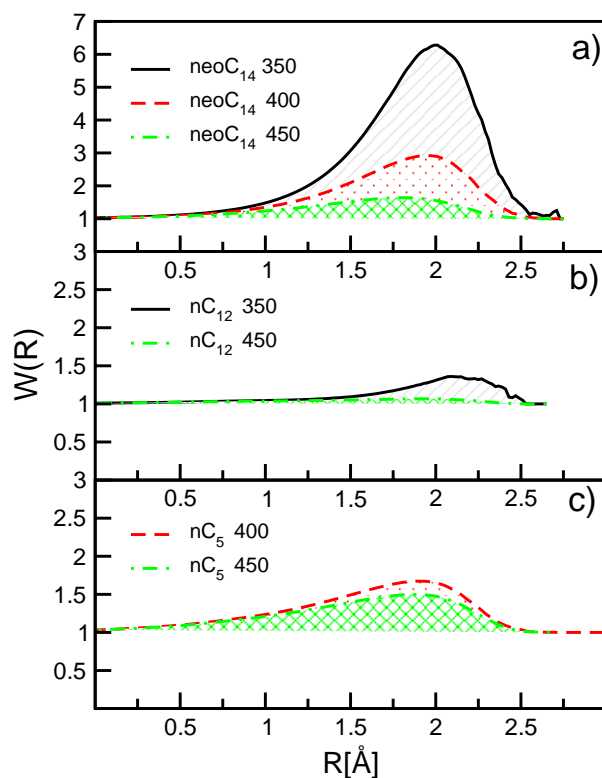
Fig. 10 Relative porosity $W(R) = \langle V(R) \rangle / \langle V_{exc}(R) \rangle$ of: a) neo-C_{14}, ; b) n-C_{12}; and c) n-C_5, at various temperatures.

increasing population of intermolecular voids, and the subsequent similarity between $\langle V(R) \rangle$ and $\langle V_{exc}(R) \rangle$, as the temperature increases. For example, in neo-C_{14} at 350 K, cage cores provide ~ 6 times more space to probes with $R \sim 2.0$Å than the spontaneous intermolecular voids do, but only ~ 1.5 times at 450 K.

Whereas ~ 100 % of the cages are empty in neo-C_{14} only 10 % are empty in n-C_{12}. Consequently, $W(R)$ is always smaller than in neo-C_{14}. In the short-tailed n-C_5 system, 30 % of cages are empty and its behaviour is intermediate between the other two systems. Compare, for example, the 450 K curves in panels a) , b) and c) of Fig. 10.

The relative porosity of n-C_5 above its melting point peaks at R $\sim$ 1.9 Å. The remaining question is whether the empty molecular cavities of this system (30 % according to Fig. 7) are able to absorb small solute molecules. In order to address this point 100 ns-long MD simulations of n-C_5 mixed with CH_4, at mole fractions of $x_{CH_4} = 0.28$, 0.44 and 0.61, were run at 400 K.[43] It was observed that the CH_4 molecules readily flowed within the liquid, visiting different cages during the course of the simulation. Also, the fraction of cages occupied by chains remained unaffected by the presence of the gas, while the mole fraction of cages occupied by CH_4 was $x_{oc}^{CH_4} =$
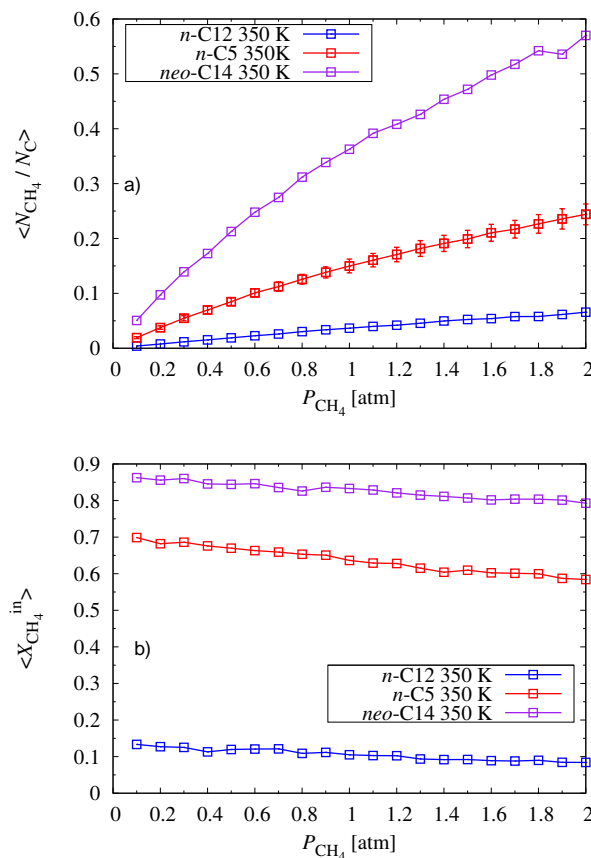
Fig. 11 a) Methane absorption isotherms in n-C_{12}, n-C_5, and neo-C_{14}, computed by Grand Canonical Monte Carlo simulations at 350 K. The amount of gas absorbed by the sample is reported as the average mole ratio $\langle N_{CH_4}/N_C \rangle$. (b) The fraction of methane molecules, $x_{CH_4}^{in} = \langle N_{CH_4}^{in}/N_{CH_4} \rangle$, located inside cages.

0.19 at x_{CH_4} =0.28; $x_{oc}^{CH_4} = 0.24$ at x_{CH_4} =0.44; and $x_{oc}^{CH_4} = 0.28$ at x_{CH_4} =0.61.[44] Consequently, even at the lowest concentration explored in our simulations, methane is able to bind to the empty cage cores. This degree of selectivity is remarkable when one considers that the cage cavities represent less than 1 percent of the total sample volume.

As a further inspection of the gas sorption properties of the systems compared in Fig. 10, the CH_4 equilibrium concentration in the liquid was computed by Grand Canonical Monte Carlo (GCMC) simulations.[45] Fig. 11a shows the methane mole ratio, $\langle N_{CH_4}/N_C \rangle$, plotted as a function of pressure in the 0.1-2.0 atm range. In the previous expression N_{CH_4} and N_C are the total number of methane and cage molecules in the sample, respectively. Fig. 11b shows the average fraction of CH_4 molecules that are inside cages, $x_{CH_4}^{in} = \langle N_{CH_4}^{in}/N_{CH_4} \rangle$, over the same pressure interval. The picture emerging from
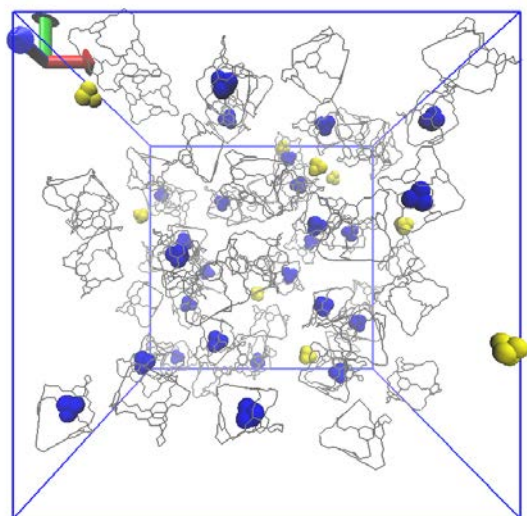
Fig. 12 Configurational snapshot of neo-C_{14} with 35 methane molecules, generated during a GCMC simulation at 350 K and 2 atm of gas pressure. Methane atoms are depicted as blue spheres whenever the molecule occupies a cage cavity.

these results is that both, methane solubility and sorption selectivity towards the cage cavities, are higher in the porous (if metastable) neo-C_{14} liquid, followed by the partially porous n-C_5 and the non-porous n-C_{12} system. The selective absorption of CH_4 in neo-C_{14} is illustrated by the simulation snapshot of Fig. 12, where CH_4 molecules bound to cage cavities are depicted in blue while the others are coloured in yellow.

7 Conclusions

We have examined the strategy of adding alkyl chains to a rigid hollow organic cage as a way to generate pure liquids with built-in microporosity. Synthetic and modelling work confirm that increasing chain length decreases the melting point from above 573 K (300 °C)[13] to as low as 313 K (40 °C), and increases the diffusion coefficient of the cages in the fluid. The fact that the diffusion coefficient increases with the molecular weight of these species confirms that it is the conformational freedom of the alkyl chains that has a decisive influence over the fluidity of the system.

Overall, the synthesis and physical characterisation of n-C_{12}, iso-C_{13}, and neo-C_{14} support some of the key conclusions from the modelling studies. Specifically, the presence of longer alkyl chains in, for example, n-C_{12} dramatically lowers the cage melting points compared to shorter chains such as in n-C_5 (ca. 40 °C versus 158 °C respectively). Also the presence of terminal branching, as in neo-C_{14}, affects the melting

and molecular dynamic characteristics of the cage, in particular increasing the melting point from ca. 40 °C to ca. 53°C.

With regard to porosity, both chain length and chain branching have been found to be important. As shown in this paper, long, unbranched chains may rapidly enter the cage cavities and thus remove the potential for permanent porosity. Terminal branching slows the rate at which tails may enter the cage, such that the system with neo-C_{14} chains has almost all cages empty for the duration of long (100 ns) simulations. For this material, free energy calculations show that occupation of the cages by the tails is, however, strongly favoured thermodynamically, meaning that the material should be regarded as a meta-stable microporous liquid. This material provides, within the time-frame of these simulations, an effective model for a liquid with permanent microporosity, which could, for example, have a similar overall structure but with larger chain terminal groups.

Regarding chain length, the presence of shorter chains, as in the n-C_5 substituted cage, results in a liquid in which 30 % of the cages are empty at any given time. Despite its relatively high melting point (429 K or 158 °C), simulations suggest that this material is, to our knowledge, the first example of a pure compound which is permanently microporous in the liquid state.

In order to understand the various aspects of liquids with permanent microporosity, we introduce relative porosity as a key parameter. This is the volume accessible to a spherical probe of radius R in the sample as a whole, relative to the volume accessible to the same probe when all the intramolecular cavities are discounted. In order to engender novel properties in porous liquids, the relative porosity should be as large as possible for relevant probe sizes. The concept of relative porosity is helpful in understanding the observed trends in methane solubility amongst some of the systems considered here.

The dissolution of methane in these materials has been modelled computationally. Methane is found to prefer to occupy the cage cavities (for materials in which these are empty) rather than the regions occupied by the alkyl chains. The methane molecules are mobile and diffuse freely between cavities during the simulations. Notably, methane is markedly more soluble in the liquids with empty cage cavities (specifically the cages with n-C_5 and neo-C_{14} chains) than in those with cage cavities which are already filled (specifically cages with n-C_{12} and n-C_{20} chains). The degree of selectivity towards the cage cavities versus the regions occupied by the tails depends, as expected, on temperature because higher temperatures generate more cavities in the intermolecular space. In general, sorption selectivity will also depend on the size of the guest molecule and its specific interactions with the cage atoms. For example, a probe like neopentane (the gas analogue of the neo-C_{14} terminal group) is expected to show

stronger binding and greater selectivity towards the cage-cores than methane, under standard laboratory conditions.

Finally, we note that the levels of absolute porosity possible in microporous solids (e.g. several tens of percent) are unlikely to be achievable in porous liquids, and therefore gas storage densities are likely to be comparatively low in comparison with porous solids. Despite this, even low absolute porosity (less than one percent) in a porous liquid dramatically affects gas solubility. The present work suggests that permanent porosity can increase gas solubility by a factor of five to ten (compare isotherms in Fig. 11). This suggests that the future for these materials may lie in new separation technologies or as tuneable reaction media.

Notes and references

1 S. Auerbach, *Handbook of Zeolite Science and Technology*, Marcel Dekker Ltd, 2003.

2 P. A. Wright, *Microporous Framework Solids*, Series: RSC Materials Monographs, 2008.

3 T. Mitra, K. E. Jelfs, M. Schmidtmann, A. Ahmed, S. Y. Chong, D. J. Adams and A. I. Cooper, *Nature Chem.*, 2013, **5**, 276–281.

4 J. T. A. Jones, D. Holden, T. Mitra, T. Hasell, D. J. Adams, K. E. Jelfs, A. Trewin, D. J. Willock, G. M. Day, J. Bacsa, A. Steiner and A. I. Cooper, *Angew. Chem. Int. Ed.*, 2011, **50**, 749–753.

5 A. Pohorille and L. Pratt, *J. Am. Chem. Soc.*, 1990, **112**, 5066–5074.

6 L. Pratt and A. Pohorille, *Proc. Nat. Acad. Sci. USA*, 1992, **89**, 2995.

7 T. L. Beck, M. E. Paulaitis and L. R. Pratt, *The Potential Distribution Theorem and Models of Molecular Solutions*, Cambridge University Press, 1st edn, 2006.

8 N. O'Reilly, N. Giri and S. L. James, *Chem. Eur. J.*, 2007, **13**, 3020.

9 T. A. Robbins, C. B. Knobler, D. R. Bellew and D. J. Cram, *J. Am. Chem. Soc.*, 1994, **116**, 111–122.

10 M. A. Little, J. Donkin, J. Fisher, M. A. Halcrow, J. Loder and M. J. Hardie, *Angew. Chem. Int. Ed.*, 2012, **51**, year.

11 S. Liu, D. H. Russell, N. F. Zinnel and B. C. Gibb, *J. Am. Chem. Soc.*, 2013, **135**, 4314–4324.

12 R. M. Fairchild, A. I. Joseph, K. T. Holman, H. A. Fogarty, T. Brotin, J.-P. Dutasta, C. Boutin, G. Huber and P. Berthault, *J. Am. Chem. Soc.*, 2010, **132**, 15505–15507.

13 N. Giri, C. E. Davidson, G. Melaugh, M. G. Del Pópolo, J. T. A. Jones, T. Hasell, A. I. Cooper, P. N. Horton, M. B. Hursthouse and S. L. James, *Chem. Sci.*, 2012, **3**, 2153.

14 P. Skowronek and J. Gawronski, *Org. Lett.*, 2008, **10**, 4755.

15 T. Hasell, X. Wu, J. Jones, J. Basca, A. Steiner, T. Mitra, A. Trewin, D. Adams and A. Cooper, *Nature Chem.*, 2010, **2**, 750.

16 See Supplementary Information.

17 B. Hess, C. Kutzner, D. van der Spoel and E. Lindahl, *J. Chem. Theory Comput.*, 2008, **4**, 435–447.

18 W. L. Jorgensen, D. S. Maxwell and J. Tirado-Rives, *J. Am. Chem. Soc.*, 1996, **118**, 11225–11236.

19 W. L. Jorgensen and J. Tirado-Rives, *Proc. Nat. Ac. Sci. USA*, 2005, **102**, 6665–6670.

20 Force-field parameters are provided as Supporting Information.

21 M. Martin and J. Siepmann, *J. Phys. Chem. B*, 1998, **102**, 2569–2577.

22 The effect of electrostatic interactions on the potential of mean force between two neo-C_7 molecules is illustrated in figure 3 of the Supplementary Information.

23 D. Holden, K. E. Jelfs, A. I. Cooper, A. Trewin and D. J. Willock, *J. Phys. Chem. C*, 2012, **116**, 16639–16651.

24 S. Jiang, K. E. Jelfs, D. Holden, T. Hasell, S. Y. Chong, M. Haranczyk, A. Trewin and A. I. Cooper, *J. Am. Chem. Soc. - ASAP article*, 2013.

25 S. Nose, *Molecular Physics*, 1984, **52**, 255–268.

26 W. G. Hoover, *Phys. Rev. A*, 1985, **31**, 1695–1697.

27 M. Parrinello, *J. Appl. Phys.*, 1981, **52**, 7182.

28 U. Essmann, L. Perera, M. L. Berkowitz, T. Darden, H. Lee and L. G. Pedersen, *J. Chem. Phys.*, 1995, **103**, 8577–8593.

29 D. Frenkel and B. Smit, *Understanding Molecular Simulation*, Academic Press, Inc., 2nd edn, 2001.

30 B. Roux, *Comput. Phys. Commun.*, 1995, **91**, 275–282.

31 S. Kumar, J. M. Rosenberg, D. Bouzida, R. H. Swendsen and P. A. Kollman, *J. Comput. Chem.*, 1992, **13**, 1011 – 1021.

32 Fitting parameters are provided as Supplementary Information.

33 The temperature dependence of the molar volumes, $V(T)$, show the same trends depicted by the $U(T)$ functions. This is discussed and illustrated in the Supplementary Information.

34 P. Ballone, C. Pinilla, J. Kohanoff and Del Pópolo, M. G., *J. Phys. Chem. B*, 2007, **111**, 4938–4950.

35 T. Cherdhirankorn, V. Harmandaris, A. Juhari, P. Voudouris, G. Fytas, K. Kremer and K. Koynov, *Macromolecules*, 2009, **42**, 4858–4866.

36 L. Bagatolli and P. S. Kumar, *Soft Matter*, 2009, **5**, 3234–3248.

37 Near the melting point the translational motion of the molecules becomes very sluggish and caging times get close to 100 ns. Consequently, the low-temperature values of D reported in Fig. 4 should be considered as lower bounds to the real, long-time average, diffusion coefficients. This observation is certainly valid for n-C_5 and neo-C_7.

38 This is illustrated in figure 3 of the Supplementary Information.

39 See figure 6 in the Supplementary Information.

40 86% of the alkyl chains visited a cage cavity during the course of a 100 ns simulation.

41 The n-C_5 simulation at 450 K was extended up to 200 ns with no drift observed in $x_{oc}(t)$.

42 The free energy was computed as $\Delta G(r) = \Delta G_{us}(r) + 2k_B T \ln(r)$, where $\Delta G_{us}(r)$ is the contribution obtained by umbrella sampling, and $2k_B T \ln(r)$ is a Jacobian correction term.

43 Simulations details and a short discussion of the main results are provided as Supplementary Information.

44 We consider that a methane molecule is inside a cage when its carbon atom is at less than 2.5 Å from the geometric centre of the cage.

45 Simulations details are provided as Supplementary Information.